Surface Wear Behavior and Friction and Wear Mechanism Studies of A356/3 wt.% Al₃Zr Composites

Hui Li, Lei Jiao, Rui Xu, Fan Li, ShengBo Lu, YuanPeng Qiao, ChuYing Li, and Pei Zhang

A direct-melt reaction was used to successfully synthesize A356/3 wt.% Al₃Zr composites at 750 °C, 770 °C and 790 °C from the Al-K₂ZrF₆ system. The friction and wear characteristics of composites synthesized at 750 ℃ were determined by carrying out dry sliding tests of varying loads and sliding speeds. Polarized light microscopy, metallurgical microscopy, x-ray diffraction, scanning electron microscopy and confocal laser scanning microscopy were applied to identify the phase compositions and observe the microstructure and morphology of the worn surfaces. Finally, the wear mechanism of composites and matrix was analyzed by observing the SEM pictures of the wear surfaces. The results indicate that Al₃Zr particles are successfully formed in the matrix. At 750℃, the particles were the smallest and dispersed well in the matrix. The size of the reinforced particles increases with increasing reaction temperature. The hardness of the composites is greatly improved compared to that of the matrix, and the highest hardness reaches 245.6 HV. The experiments show that the friction coefficient of the composites is lower than that of the matrix, and the smallest average friction coefficient is 0.367. The volume wear loss of the composites is less than that of the matrix. The wear mechanism of composites is mainly adhesive wear and is accompanied by abrasive wear and fatigue wear because of the change in experimental parameters. Eventually, delamination wear occurs, and the wear resistance is better than that of the matrix.

1. Introduction

Particle-reinforced aluminum matrix composites (PRAMCs) have attracted appreciable interest for their applications in the military, aerospace and automobile industries by virtue of their unique properties, such as low density, good thermal stability, high wear resistance and better economic viability than steel and aluminum alloys (Ref 1-5). Ceramic particles such as Al₂O₃, SiC, B₄C, Al₃Zr, TiB₂ and ZrB₂ are commonly used to enhance their performance (Ref 6-9). Among them, Al₃Zr particles were proven to be an ideal reinforcement that can hinder the recrystallization process and refine the crystal structure and can also change the primary α-Al crystal from coarse branches to fine equiaxed crystals (Ref 10,11). There are many methods for the fabrication of PRAMCs, including stir casting, powder metallurgy, squeeze casting and direct-melt reactions (Ref 12-15). The direct-melt reaction (DMR) is a potential method for fabricating PRAMCs because it can incorporate the particles into semisolid aluminum, be used in casting and also transform the dendritic phase into a spherical phase such that micro- and nanoparticles can be stirred in a

highly viscous melt (Ref 15). The in situ AMCs synthesized by DMRs have superior clean interfaces, strong interfacial bonding, good thermodynamic stability and better economic feasibility than ex situ AMCs (Ref 16-19).

Friction and wear properties are important performance indicators of composite materials (Ref 20). In addition, many studies have been done. CHEN Deng-bin et al. found that the wear loss of composites was significantly reduced under the same experimental conditions. As the volume fraction of particles increases, the wear resistance of the composites gradually increases (Ref 21). Moreover, Abhishek Kumar et al. found that the addition of TiC particles to the composites made them more wear resistant than pure aluminum (Ref 22). Furthermore, Fei Chang et al. studied the effect of SiC particle size on in situ (Al₄SiC4+SiC)/Al composites and found that fine particles improved the wettability of the reinforcement to the matrix. Compared to materials reinforced with coarse SiC particles, fine SiC particles reduced the friction coefficient by 19% and the wear rate by 66% (Ref 23). TENG Jie et al. found that the wear rate of Al-Si/SiC composites increases with increasing load and decreases with increasing Si content in the matrix (Ref 24). In addition, Jiao Lei et al. found that as the amount of forging deformation increases, the friction coefficient of the composite material increases first and then decreases, the worn surface roughness decreases, the width of the wear scar becomes wider and the depth becomes shallower (Ref 25).

Previous studies have studied the effect of particle content, particle size, applied loads and forging on the friction and wear properties of composites. However, there are few studies on the effect of the reaction temperature on composite materials. Based on this, in this study, A356/3 wt.% Al₃Zr composites were successfully synthesized at different reaction temperatures

Hui Li, ShengBo Lu, YuanPeng Qiao, and **ChuYing Li**, School of Materials Science and Engineering, Jiangsu University of Science and Technology, Mengxi street, Zhenjiang 212003, People's Republic of China; **Lei Jiao, Rui Xu, Fan Li,** and **Pei Zhang**, School of Material Science and Engineering, Jiangsu University, Xiangshan street, Zhenjiang 212013, People's Republic of China. Contact e-mails: jiaolei@ujs.edu.cn and 973170727@qq.com.

(750 °C, 770 °C, 790 °C) from the Al-K_2ZrF_6 system by a direct-melt reaction. Based on the microstructure and morphology of the three different composites, the composites synthesized at 750℃ were selected for friction and wear performance comparison with A356.

2. Experimental Procedures

2.1 Material Preparation

Commercial A356 aluminum alloy ingots were taken as the matrix alloy, and their composition is shown in Table 1. Pure potassium fluorozirconate (K_2ZrF_6) powder was selected as the reactant source to synthesize A356/3 wt.% Al_3Zr composites at different reaction temperatures (750℃, 770℃, 790℃) by reaction Eq 1:

$$3K_2ZrF_6 + 13Al = 3Al_3Zr + 3KAlF_4 + K_3AlF_6 \quad (Eq\ 1)$$

First, experimental inorganic salt K_2ZrF_6 powder was dehydrated at 200 °C for 3 hours in an electric furnace and wrapped in aluminum foil. Then, 1200 g of A356 aluminum alloy and 40.6 g of K_2ZrF_6 powder were weighed according to the mass of the added Al_3Zr particles to achieve a content of 3 wt.% after calculation. When the temperature of the aluminum melt was set to 750 °C, 770 °C and 790 °C, aluminum foils with dried powers were added. A campanulate graphite plunge was used to introduce the salt mixture into the aluminum melt to avoid salt floatation, and a graphite rod was used for mechanical stirring. After 10 minutes of reaction, the mechanical stirring device was removed, a refining agent was added, the slag was refined for 5 minutes, and the slag was scraped. After cooling to 720 °C, the melt was poured into the prepared copper mold and cooled to room temperature.

2.2 Tests and Analysis

The dry sliding wear test was conducted using a UMT-2 wear tester, and the friction pair was Al_3O_2 hard balls with a diameter of 10 mm. For the friction and wear test, the A356/3wt% Al_3Zr composites prepared at 750 °C were selected and compared with the A356 aluminum alloy. The shape of the test samples is a 15×15×3 block, and the wear surface is a 15×15 plane that was mechanically polished (unit: mm). There are two experimental groups in total, one of which applies the same sliding speed (250 rev/min) and different loads (samples 1, 2, 3 and 4) and the other applies the same load (5 N) and different sliding speeds (samples 5, 2, 6 and 7). The wear scar diameter of the samples was 6 mm, and the test time was 30 minutes. Other experimental parameters are shown in Table 2.

After the friction and wear experiments, a confocal laser scanning microscope (model LEXT OLS4000) was used to observe the microstructure of the worn surfaces and determine their cross-sectional area simultaneously. Then, the average of the measured cross-sectional area results was taken, and the volume wear loss (mm³) was calculated by Eq 2:

$$Volume\ wear\ loss = C \times S \quad (Eq\ 2)$$

where C is the wear circumference (mm) and S is the wear cross-sectional area (mm²).

The microstructure and morphology of the materials and their worn surfaces were observed by metallurgical microscopy (model HAL1000) and polarized light microscopy (model Leica750P) and SEM (model ZEISS Merlin Compact). The compositions of the prepared composites were analyzed using XRD (model XRD-6000) and EDS. A Vickers hardness tester (model KB30S) was used to test the hardness of the materials.

3. Results and Discussion

3.1 XRD Analysis

The XRD patterns of the A356/3 wt.% Al_3Zr composites obtained by the methods described before are shown in Fig. 1. This indicates that the Al_3Zr reinforcement phase is successfully obtained. The diffraction peak shifted slightly to the left. This is because the volume of the reinforced particles increases, which means that the hybrid becomes more serious for the matrix, and the lattice constant and the interplanar spacing increase simultaneously as the reaction temperature increases. In addition, as the temperature rises, the intensity of the Al diffraction peak gradually weakens because Al is continuously consumed as a reactant in the reaction system.

Combining reaction Eq 1 of the reaction system in this experiment with the second law of thermodynamics gives following Eq 3:

$$\Delta G = \Delta H - T\Delta S \quad (Eq\ 3)$$

The reaction can proceed spontaneously only when the Gibbs free energy of the reaction system decreases. Substituting each data point (Ref 26) into the formula of Gibbs free energy gives □G of 2508.779 J/mol at 750℃, which is negative, indicating that the reaction used in this experiment can proceed spontaneously and confirming the formation of the Al_3Zr reinforcement phase again from the perspective of thermodynamics.

3.2 Microstructures

The microstructures of the prepared composites observed by polarized light microscopy are shown in Fig. 2(a–d). The grains are uniformly distributed in the composites. Furthermore, with increasing reaction temperature, the growth trend of grains is obvious. The difference in the grain size of different materials will lead to different performances. The average grain sizes and standard deviations of the composite material at 750°C, 770°C and 790°C and A356 are 130±20, 190±25, 180±20 and 204±25 μm, respectively. The minimum value is that of the composites prepared at 750℃, 130±20 μm.

Table 1 Nominal composition of the A356 ingots/wt.%

Elements	Si	Mg	Fe	Mn	Zn	Ti	Cu	Pb	Al
Weight%	6.5–7.5	0.2–0.4	≤0.2	≤0.1	≤0.1	≤0.2	≤0.05	≤0.0.05	Bal

Table 2 Parameters of friction and wear experiments

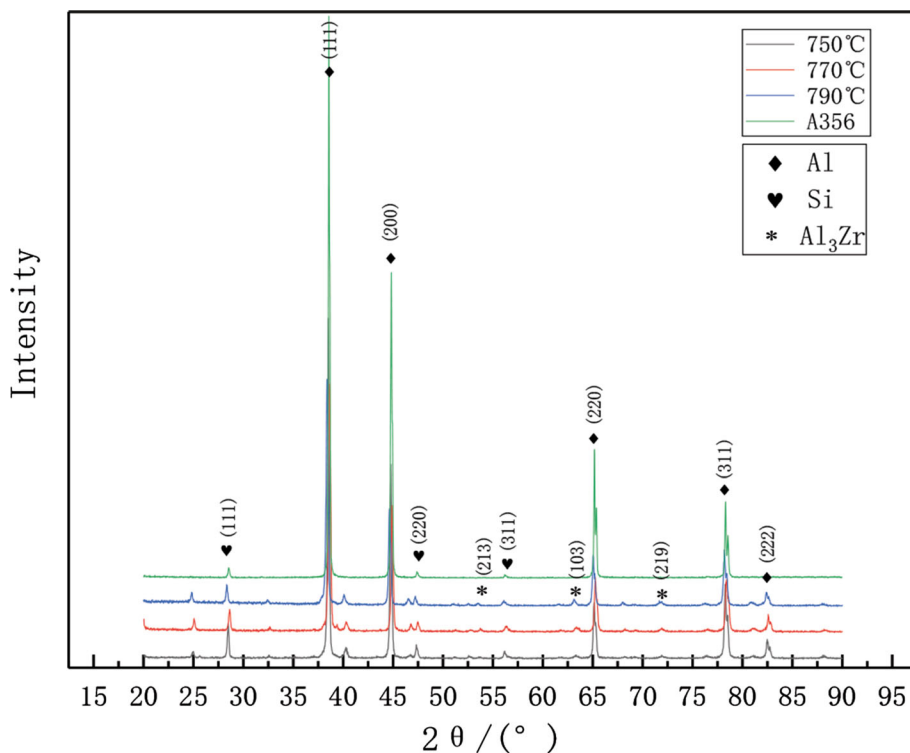| Group	Sample	Applied loads, N	Sliding speeds, rev/min
I	1	3	250
	2	5	250
	3	7	250
	4	9	250
II	5	5	150
	2	5	250
	6	5	200
	7	5	300

Fig. 1 XRD patterns of the A356/3 wt.% Al$_3$Zr composites at different reaction temperatures

Figure 3(a–c) shows the metallographs of the three composites. From Fig. 3(a–c), the Al$_3$Zr particles are mostly distributed at the grain boundaries and rarely appear inside the grains, and a small number of them agglomerate. When the reaction temperature is 750 °C, the Al$_3$Zr particles are granular and exhibit short rod shapes with a size of approximately 15 μm; when the temperature rises to 770℃, a long slat-shaped distribution occurs. Compared with the 750 °C sample, the extent of the aggregation phenomenon is reduced, and particle growth is obvious. Afterward, when the temperature continued to rise to 790 °C, the size and shape of the reinforced particles varied, with shapes including long slats and short rods. Consequently, the shape of the particles is related to the reaction temperature. This change occurs because with the increase in the reaction temperature during in situ preparation, the atomic diffusion coefficient increases, grain boundary migration becomes easier, and the grain boundary energy decreases, thereby leading to the spontaneous growth of the particles.

The SEM and EDS results of the A356/3wt% Al$_3$Zr composites prepared at 750 °C are shown in Fig. 4(a–b). In Fig. 4(a), the Al$_3$Zr-reinforced particles are gray, and the black background is the A356 matrix. Afterward, Fig. 4(b) indicates the results of the EDS spectrum of point A in Fig. 4(a) and shows that in addition to the Si of A356, only Zr and Al are present in the particle. This result is consistent with the XRD results and proves that the reinforced particles in the composites are Al$_3$Zr particles.

3.3 Mechanical Properties

3.3.1 Hardness. Figure 5 shows the micro-Vickers hardness of the A356 matrix and A356/3 wt.% Al$_3$Zr composites prepared at different reaction temperatures. Compared with that of the A356 aluminum alloy, the microhardness of the prepared composites was greatly improved, which indicates that the strengthening effect of the reinforced particles was significant. The hardness is the highest at 750 °C, reaching 245.6 HV. In contrast, the hardness of the composites at 770 °C and 790 °C
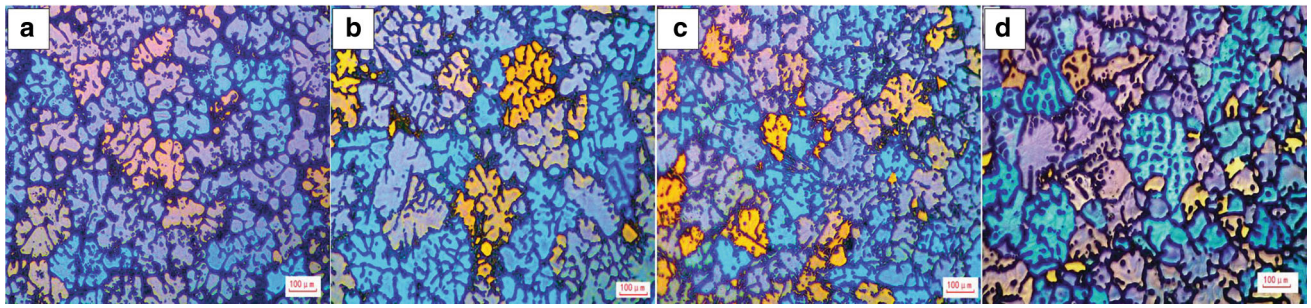
Fig. 2 Polarized light microscopy images showing the microstructures of A356/3 wt.% Al₃Zr composites prepared at (a) 750 °C, (b) 770 □, (c) 790 □ and (d) A356
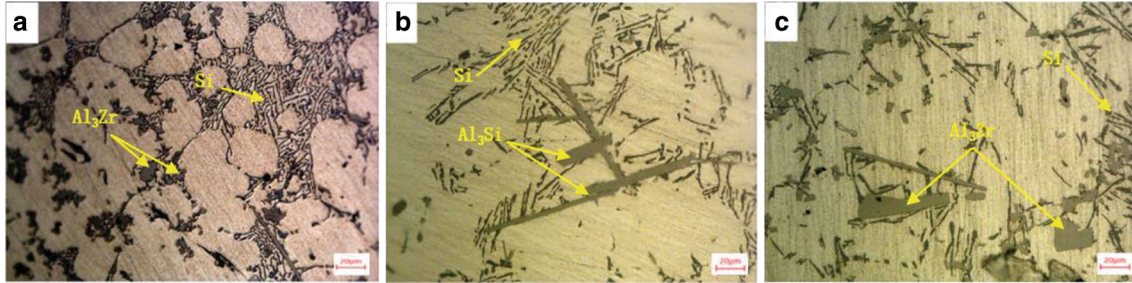

Fig. 3 Metallographs of the A356/3wt% Al₃Zr composites prepared with different reaction temperatures: (a) 750 □, (b) 770□ and (c) 790 °C
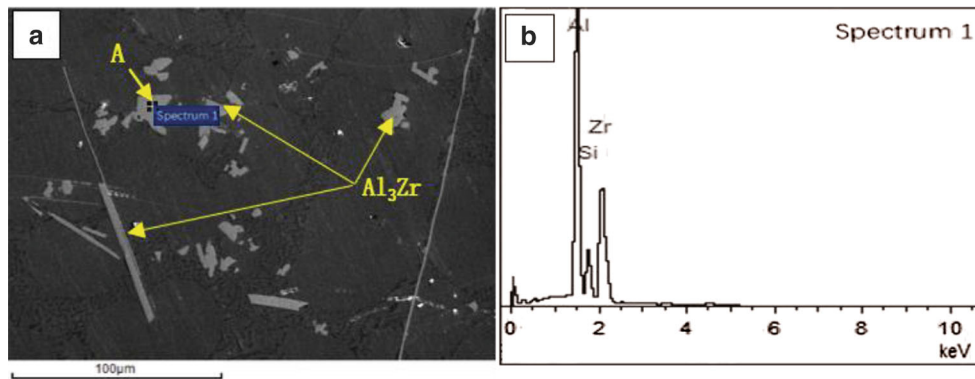

Fig. 4 SEM and EDS results of the A356/3 wt.% Al₃Zr composites prepared at 750 °C: (a) SEM image and (b) EDS spectrum of point A in (a)

decreased slightly. The results of the polarized light microscopy and metallographs show that the decrease in hardness is due to the Al₃Zr particles growing gradually and the extent of the dispersion decreasing because of the rising temperature. When the temperature is 750 °C, the reinforced particles are small and dispersed. This makes the crystal grains smaller, which has the effect of fine grain strengthening and also hinders dislocation slip. When the particles are enlarged, the fine grain strengthening and dislocation pinning effects will weaken. Thus, the hardness of the materials decreases absolutely. Because the hardness of the composites prepared at 750℃ is the highest, friction and wear performance analysis is performed on this composite and compared with the A356 aluminum matrix.

3.3.2 Friction Coefficient. The friction coefficient reflects the characteristics of the wear pair in the experiments and is affected by various factors, such as load, temperature and

sliding speed (Ref 27). The friction coefficient curve is shown in Fig. 6(a–f). The friction coefficient curve of composites with the same sliding speed (250 rev/min) and different loads (3 N, 5 N, 7 N and 9 N) is shown in Fig. 6(a), and the friction coefficient curve of the A356 aluminum matrix under the same conditions is shown in Fig. 6(d). Because the testing surface of the sample is sanded and polished with sandpaper, the surface is smooth, so the friction coefficient is very low within a few seconds of the start; however, as the surface becomes rough, the friction factor increases rapidly (Ref 28,29). Only when the applied load reaches 9 N does the friction coefficient fluctuate significantly, and the fluctuation increases with the passage of time, as shown in Fig. 6(a). This is because new abrasive debris and hard particles constantly fall off the surface in the experiment, which will cause a large change in surface roughness and then cause large fluctuations. When the friction

time is over half, the curve generally shows an upward trend. This is because with increasing friction time, cracks appeared on the surface, resulting in an increase in the surface roughness and friction coefficient. Figure 6(d) shows that the friction coefficient of each group in the first half fluctuated greatly, and the friction coefficient showed a rough downward trend. This is because there is a large amount of abrasive debris at the beginning, which will continuously change the roughness of the friction surface. As friction progresses, the production of alumina will be accelerated, which will make the surface smoother and more wear resistant. This is the main reason for the decline in the coefficient. The friction coefficient of each group in the second half of the time tends to stabilize, and it

also shows an upward trend like the composites. This is because by this stage, a large number of cracks, spalling layers and wear debris appeared on the friction surface, cracks continued to expand, and wear debris continued to accumulate as the experiment progressed.

The friction coefficient curves of the A356 aluminum matrix and composites with the same load (5 N) and different sliding speeds (150 rev/min, 200 rev/min, 250 rev/min and 300 rev/min) are shown in Fig. 6(b) and (e). As presented in Fig. 6(b), the friction coefficient of most curves increases rapidly after the initial wear and then decreases and maintains a stable level. Only when the speed is 150 rev/min does the curve decrease and then rise to maintain a stable level. This is because the matrix is softer than the reinforced particles in the running-in phase of friction. Therefore, the matrix is first worn away by the friction pair, which then produces furrows and abrasive debris, leading to harder reinforced particles remaining and floating on the surface and forming protrusions that contact the friction pair. Therefore, the friction coefficient is large in the initial stage. After that, friction enters a stable stage. The rate of the appearance of abrasive particles on the surface is approximately the same as the transfer rate, so the friction coefficient can be maintained in a stable range, resulting in a small friction coefficient. In Fig. 6(e), all the curves decrease and then maintain a stable level after the friction coefficient increases rapidly at the beginning. At first, the friction coefficient is particularly small because the sample is polished, and abrasive debris starts to rapidly increase the friction coefficient as friction starts. Subsequently, the friction coefficient is reduced due to the generation of alumina, and the appearance of debris and its transfer rate reach a balance, which shows that the friction coefficient becomes stable. Comparing Fig. 6(b) and (e), it was found that the friction coefficient is the largest when the applied sliding speed is 150 rev/min. When the rotation speed is slow, the sample enters the severe friction stage after a
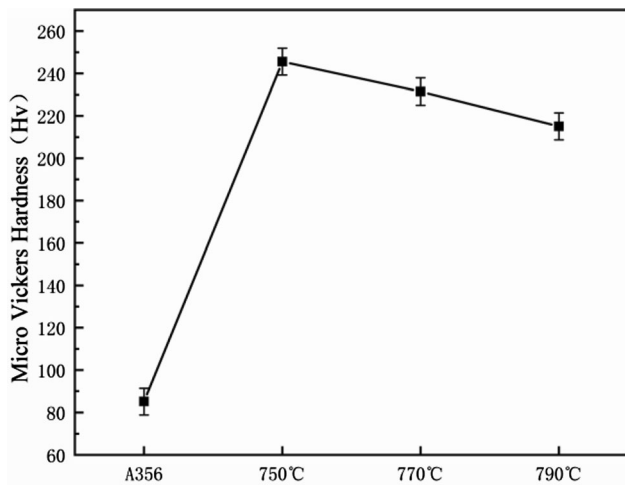

Fig. 5 Micro-Vickers hardness of the A356 matrix and A356/3 wt. % Al$_3$Zr composites at different reaction temperatures
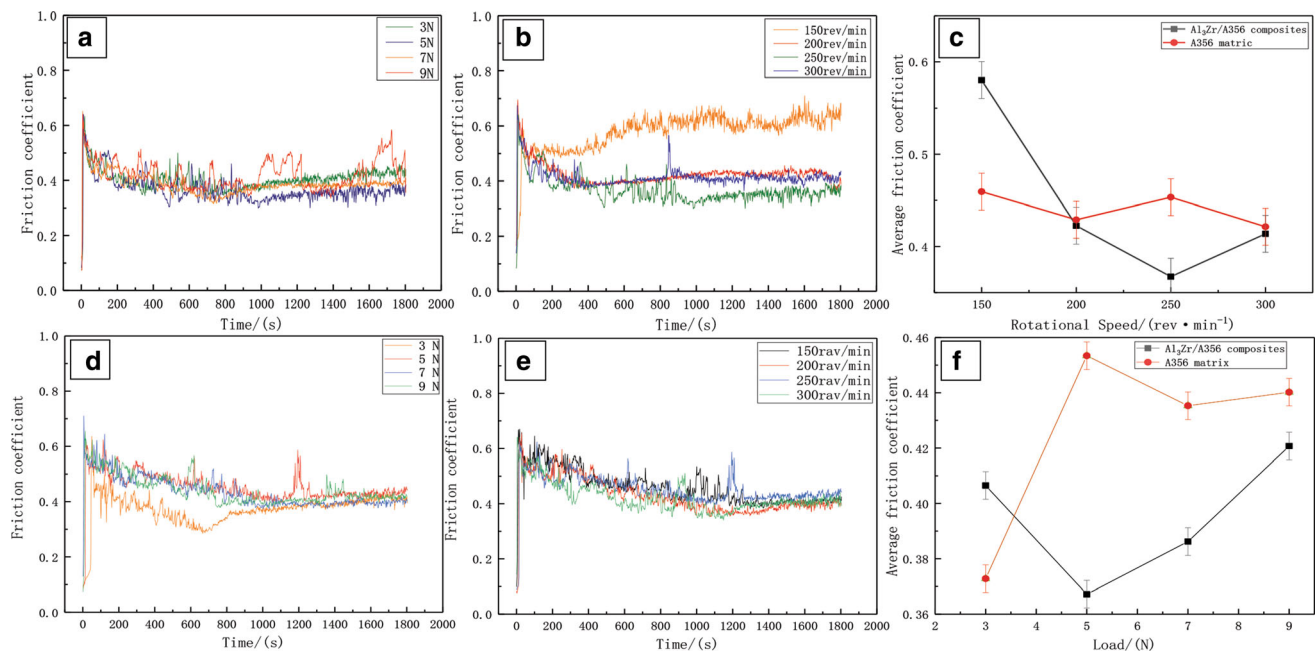

Fig. 6 Friction coefficient results: (a) A356/3 wt.% Al$_3$Zr composites and (d) the A356 matrix with a sliding speed of 250 rev/min; (b) A356/ 3 wt.% Al$_3$Zr composites and (e) the A356 matrix with a load of 5 N; and the average friction coefficient of different materials with (c) the same sliding speed of 250 rev/min applied and different loads and (f) the same load of 5 N and different sliding speeds
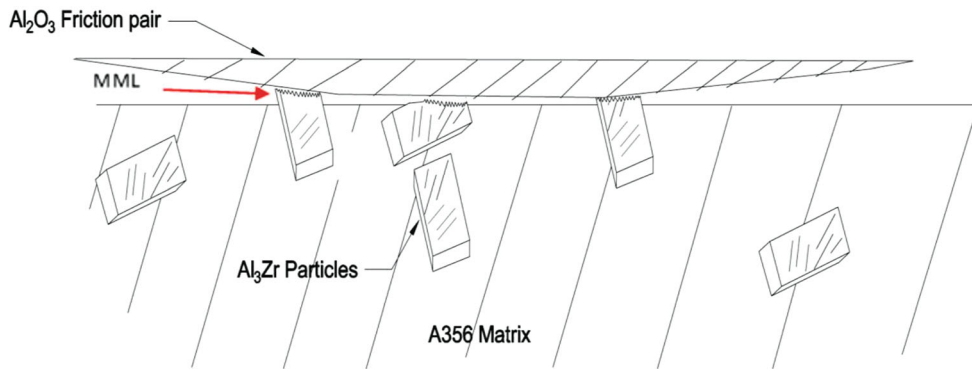
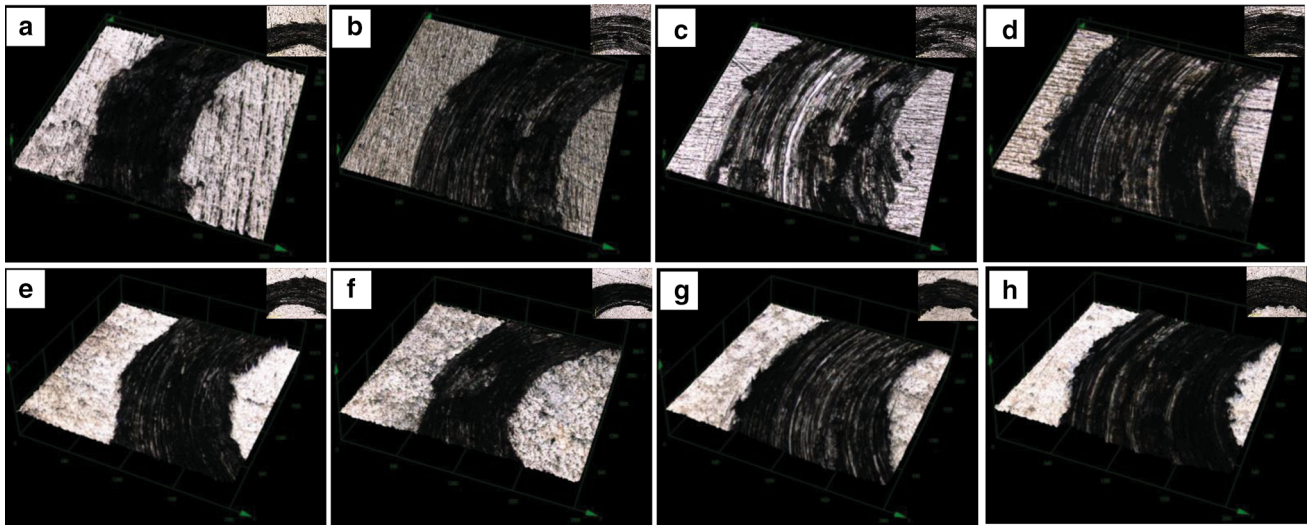**Fig. 7** Friction and wear model diagram of composites

Fig. 8 Laser confocal microscopy images of different materials with the same sliding speed of 250 rev/min. Results of the A356 matrix (a)∼(d) with different applied loads: (a) 3 N, (b) 5 N, (c) 7 N and (d) 9 N. Results of the A356/3 wt.% Al$_3$Zr composites (e)∼(h) with different applied loads: (e) 3 N, (f) 5 N, (g) 7 N and (h) 9 N

short time. At this time, there is a large surface roughness and severe surface vibration, and the friction coefficient increases. When the sliding speed is faster, the time required for the running-in phase and friction coefficient to stabilize is longer. In addition, severe fluctuations in the friction coefficient occur when the sliding speed is 250 rev/min or 300 rev/min.

Figure 6(c) and (f) shows the average friction coefficient of different materials and indicates that the average friction coefficient of A356/3 wt.% Al$_3$Zr composites decreased first and then increased in both experimental groups. The friction coefficient obtained with an applied load of 5 N and sliding speed of 250 rev/min was the smallest of all groups and was 0.367. The decrease in the average friction coefficient is due to the increase in the applied load, which causes the temperature of the friction surface to increase and accelerate the formation of an oxide film, thereby reducing the friction coefficient (Ref 28). When the applied load exceeds 5 N, the average friction coefficient rises significantly. This is because the wear debris and hard particles generated during the friction process are pressed into the surface of the composites under the normal shear stress of the larger load, which leads to a large plowing contribution and rising friction coefficient. In contrast, the

average friction coefficient of the A356 matrix is relatively stable based on these two figures. Only when the load is 3 N is the friction coefficient the smallest, 0.372. By comparison, the friction coefficient of the A356 matrix is higher than that of the composites. The small value at 3 N may be caused by improper experimental operation. The reason why the friction coefficient is smaller is that the Al$_3$Zr particles are ground into finer powder particles during the friction process. Thus, they form a local micro-protruded layer at the friction place. These hard and micro-protruded Al$_3$Zr particles are in direct contact with the friction pair, reducing the contact area between the softer matrix and the friction pair protecting the surface of the materials.

The friction and wear model diagram of the composites are shown in Fig. 7. From this diagram, a mechanically mixed layer (hereinafter referred to as MML) on the friction surface is completely different from the original state after friction starts. When a thin MML with a high hardness forms, the friction properties of the material can be improved (Ref 30). The MML formed by the hard Al$_3$Zr particles can achieve this effect. When the Al$_3$Zr particles in the material are rubbed, the MML with micro protrusions can reduce the frictional contact surface area and even have a certain lubricating effect so that the
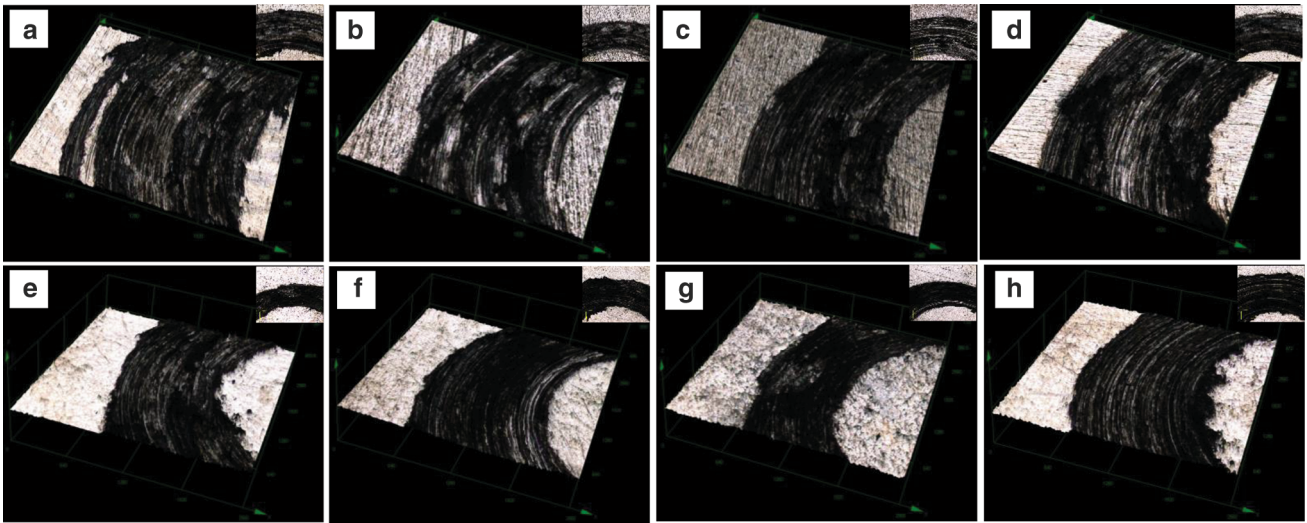
Fig. 9 Laser confocal microscopy images of the different materials with the same load of 5 N applied. Results of the A356 matrix (a)∼(d) with different sliding speeds: (a) 150 rev/min, (b) 200 rev/min, (c) 250 rev/min and (d) 300 rev/min. Results of the A356/3wt% Al₃Zr composites (e)∼(h) with different sliding speeds: (e) 150 rev/min, (f) 200 rev/min, (g) 250 rev/min and (h) 300 rev/min
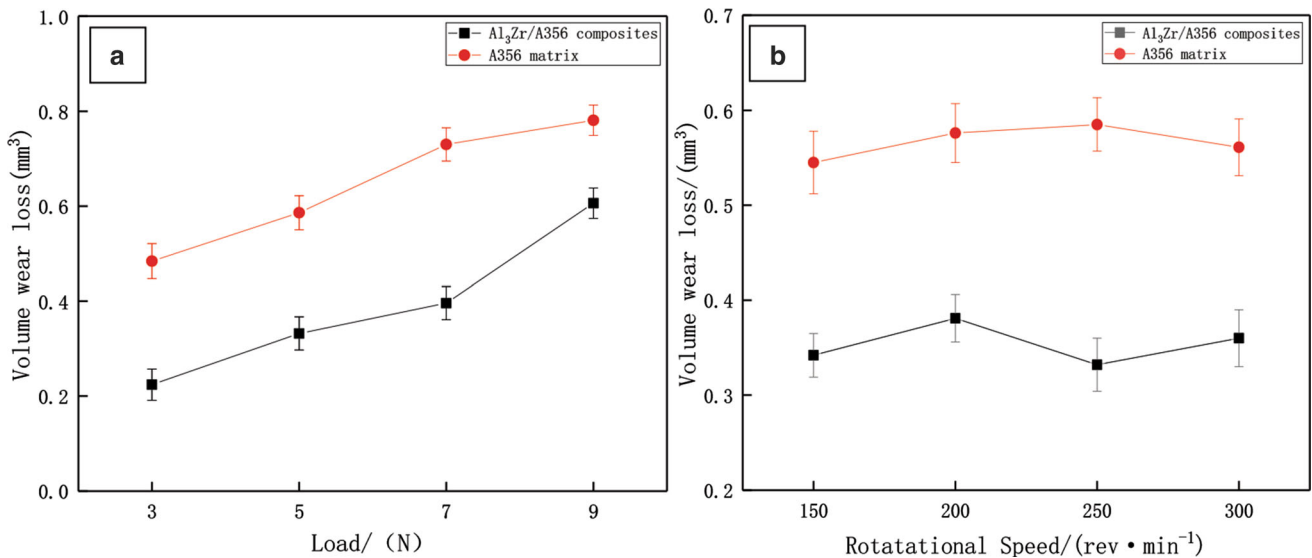

Fig. 10 Wear volume loss curve: (a) the same sliding speed of 250 rev/min and (b) the same load of 5 N

friction coefficient decreases and becomes stable. This coincides with the change in the friction coefficient analyzed above, which proves once again that the Al_3Zr particles in the composites can improve the friction properties of the material.

3.3.3 Wear Volume Loss. Figure 8(a–h) is laser confocal microscopy images of different materials with a constant sliding speed (250 rev/min) and different loads (coordinate length unit: μm) applied. From Fig. 8(a–d), it can be seen that for the A356 matrix, as the load increases, the cross-sectional area of the worn surface increases, the wear scars deepen, and the wear scars around the worn circumference gradually become clear. By comparing Fig. 8(e) and (h), we can clearly see that the worn surface is significantly enlarged when the load is 9 N. As shown from Fig. 8(e–f), as the load increases, the wear area also increases. Figure 9(a–h) is the laser confocal microscopy images of material with a constant load (5 N) and

different sliding speeds (coordinate length unit: μm) applied. The figure shows that as the speed increases, the cross-sectional area of the worn surface increases, the wear depth becomes shallower, and the wear scars are clearer. Comparing the two different materials, the wear area of the A356/3 wt.% Al_3Zr composites is significantly reduced. Therefore, the materials reinforced by Al_3Zr particles have better wear-resistance properties, and the particles prepared by the in situ reaction are beneficial to the composites during the wear process (Ref 31).

Figure 10(a–b) is graph of the wear volume loss of two different materials under variable load and sliding speed experimental conditions. The formula used to calculate the amount of wear volume loss is Eq 2.

As shown in Fig. 10(a), with increasing load, the wear volume loss of the two materials shows a rapid increasing
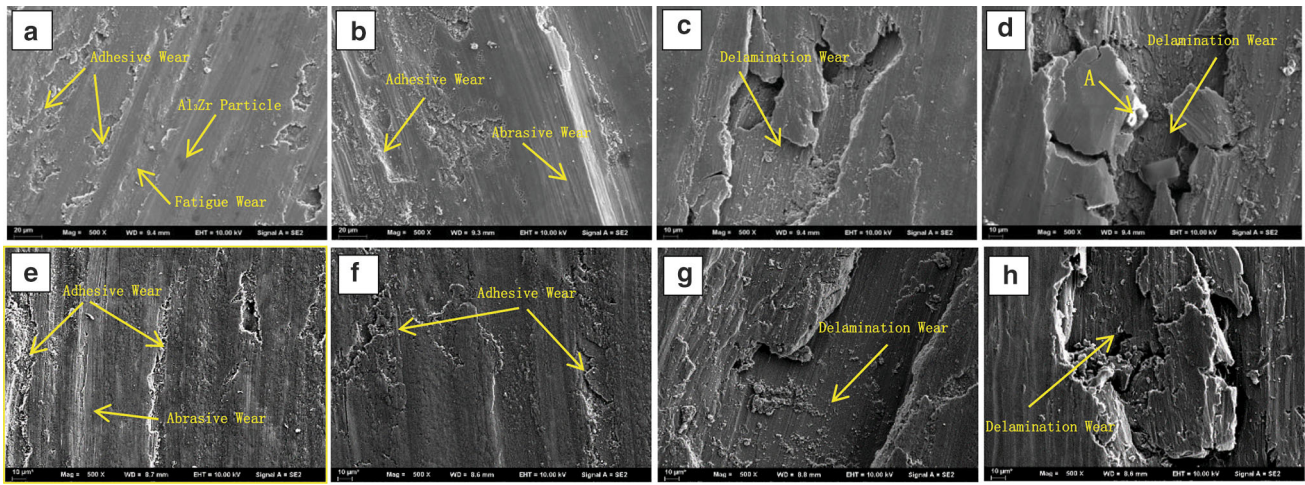
Fig. 11 SEM results of the worn surfaces. Worn surfaces of A356/3 wt.% Al$_3$Zr composites with different applied loads (a)~(d): (a) 3 N, (b) 5 N, (c) 7 N and (d) 9 N. Worn surfaces of A356 composites with different applied loads (e)~(h): (e) 3 N, (f) 5 N, (g) 7 N and (h) 9 N

trend, but the wear loss of the composites is lower than that of the A356 alloy because harder Al$_3$Zr particles are used as the carrier and can help reduce wear during the wear process. From Fig. 10(b), the wear volume loss of the two materials shows a gradually increasing trend with the increase in the sliding speed, which is different from the change shown in Fig. 10(a) and indicates that the impact of the load on the wear volume loss is relatively more obvious than that of the sliding speed on the wear volume loss. From Fig. 10, it can be seen that the reinforced composites are more wear resistant than the A356 alloy. The change in wear loss increases with increasing speed and load. According to Eq 2, the result is consistent with the conclusion that the wear area increases with increasing sliding speed and load, as shown in Fig. 9.

3.3.4 Wear Mechanisms. Figure 11 shows the SEM results of the worn surfaces of two materials with the same sliding speed of 250 rev/min and different loads applied. Figure 11(a–d) shows that there are furrows and flaky spalling pits on the worn surface, and the worn surface undergoes obvious plastic deformation. In Fig. 11(a), when the experimental load is 3 N, the wear is the slightest. The worn surface is shallow, and the peeling area is small. At this time, the wear mechanism is mainly adhesive wear (Ref 32) and slight fatigue wear, which is due to the mutual engagement between the composites and the friction pair. From Fig. 11(b), with unchanged sliding speed and increasing the load to 5 N, the wear mechanism is changed to abrasive wear and severe adhesive wear. The area of the spalling pits has increased relative to that shown in Fig. 11(a), and abrasive wear caused by abrasive debris has appeared, which indicates that the increase in load conditions worsens the material wear. Figure 11(c) and (d) shows that a large number of pits and flakes have begun to appear on the worn surface, internal cracks are obvious, there is a tendency to continue to expand, and there are hard particles in the spall pit. Therefore, the wear mechanism is delamination wear at this moment. In the process of wear, when the friction pair is in contact with the worn surface, friction force will be generated between the two, and external work is done, resulting in friction heat formation. In addition, under the action of heat, the worn surface is deformed. When the deformation is severe, the deformation will cause a plowing phenomenon, and an adhesion point will

be formed. Adhesive points fell off, debris appeared because of the shearing force, and the wear mechanism was adhesive wear. With the passage of time, the adhesion point grows, and the matrix peels off as lamellae under the action of large shear forces, which causes severe delamination wear. Moreover, the worn surface easily reacts with oxygen so that Al in the matrix is oxidized to form an oxide film. Point A in Fig. 11(d) is likely to be alumina.

The SEM images of the A356 alloy with the same experimental parameters are shown in Fig. 11(e–h). When the load is low, the wear mechanism is mainly adhesive wear and abrasive wear and compared with the worn surface of composites under the same experimental conditions, the wear loss and the area of the spalling pit of the A356 alloy significantly increased, as shown in Fig. 11(e) and (h). From Fig. 11(g) and (h), when the loads rise to 7 N and 9 N, the wear mechanism changes to more severe delamination wear, and the area of delamination increases obviously. This is because the A356 alloy with low hardness will cause worse wear and produce much wear debris.

In summary, comparing the SEM images of the worn surfaces of the composites and matrix alloy shows that the composites are more wear resistant. This is because the hard Al$_3$Zr particles bear the load and can bridge expansion because of their close combination with the matrix during the process of crack generation. In addition, the bridged linkage makes it so that cracks must bypass the reinforced particles and consume energy, thereby slowing down or even preventing crack expansion. Moreover, the temperature of the worn surfaces increased rapidly during the wear process, which caused the softer A356 matrix to soften quickly and begin to move and agglutinate on the surface, eventually causing adhesive wear. However, the Al$_3$Zr particles could hinder the flow of the matrix and reduce the cutting effect of the friction pair on the surface. Simultaneously, the shear strain resistance property of the composites is improved, which is beneficial for forming a transfer film and reducing the adhesion area of the worn surface.

Figure 12 and 13 shows the SEM and EDS results of the composite worn surfaces. Figure 12(a–d) shows SEM images of the worn surfaces of composites with different sliding speeds
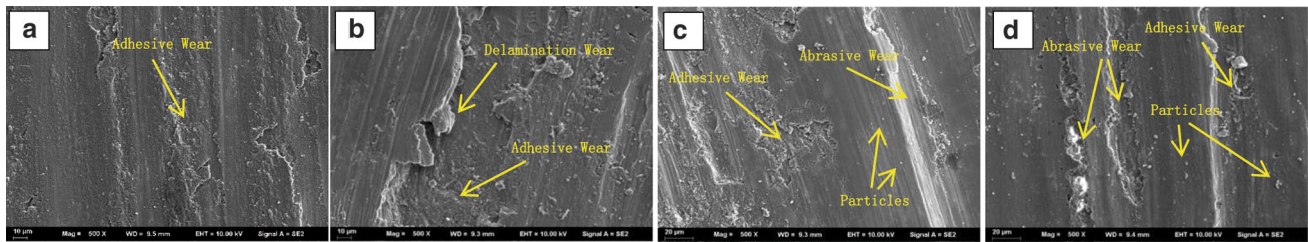
Fig. 12 SEM and EDS results of composite worn surfaces with the same load of 5 N and different sliding speeds of (a) 150 rev/min, (b) 200 rev/min, (c) 250 rev/min and (d) 300 rev/min
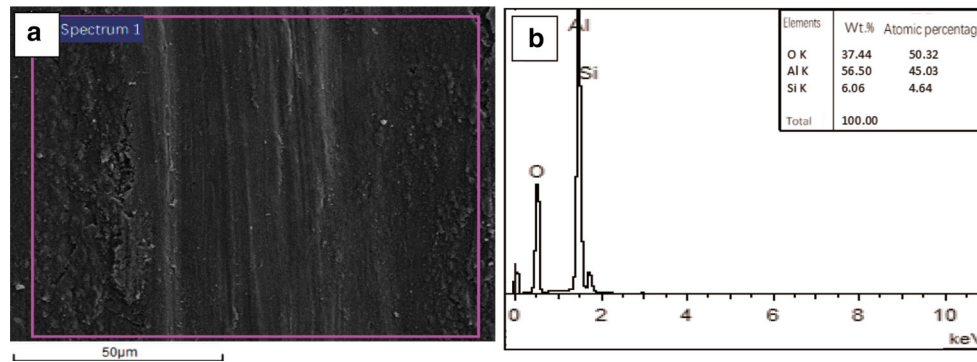

Fig. 13 EDS results of composite worn surfaces with a load of 5 N and sliding speed of 300 rev/min: (a)–(b)

and a constant load of 5 N. Traces of plastic deformation on the worn surface are generated, and furrows and grooves exist along the wear direction. In addition, combined with the EDS results, the worn surface was rich in oxygen, so an oxide film appeared on the worn surface. Figures 12(a) and (b) shows the surfaces with sliding speeds of 150 rev/min and 200 rev/min, and the wear mechanism mainly manifests as adhesive wear and causes delamination wear. Furrows appeared on the worn surface and were generated because the surface was uneven. Furthermore, the surface undergoes plastic deformation to produce raised adhesion points due to the effects of friction. The cutting force at the adhesion location increases so that the surface material falls off along the wear direction, with furrows and cutting marks gradually occurring. As time passes, the adhesion points grow and cause lamellar spalling due to the large shear forces. The oxide film is partially lifted but is subsequently pressed into the worn surface by the friction pair, resulting in a large number of cracks. The sliding speeds of Fig. 12(c) and (d) are 150 rev/min and 200 rev/min, respectively. In these two figures, the furrows on the worn surface become shallower, the oxide film is destroyed, the extent of lamellar shedding is reduced, and hard particles are obviously present on the worn surface. At this time, wear occurs by the mechanisms of abrasive wear and adhesive wear. The friction pair broke the oxide film, and the worn composites were exposed. After that, the relatively soft matrix was quickly worn away because of shear force, exposing the harder reinforced particles and dividing the adhesion points into discontinuous points. At this time, not only adhesive wear but also abrasive wear caused by hard particles occur on the worn surface. As presented in Fig. 13, the SEM image combined with the EDS spectrum shows that the worn surface is rich in oxygen, which shows that an oxide film formed on the worn surface during the wear process.

These oxide films form due to oxygen being involved in the friction pair and the wear sample under high-speed rotating friction and then reacting with Al in the matrix. When the speed increases, due to the influence of frictional heat, oxidative wear will turn into adhesive wear, which will dramatically increase the extent of wear. An increase in temperature usually increases oxidative wear. When working in an oxidizing medium, the oxide film on the surface of the workpiece will be reformed after being worn. The shear strength at the junction of the oxide film and the substrate is high, and when the wear rate of the oxide film is greater than the rate of formation of the oxide film, the extent of wear is large; in contrast, when the shear strength of the junction between the oxide film and the substrate is high or when the wear rate of the film is lower than the formation rate of the oxide film, the extent of wear on the oxide film is small, and the oxide film can have a good anti-wear effect.

4. Conclusions

(1) When the reaction temperature was 750℃, the composites contained small, short rod-shaped reinforced particles dispersed in the A356 matrix. With increasing reaction temperature, the morphology of the Al_3Zr-enhanced particles gradually changed from short bars to strips, and the dispersion extent worsened.

(2) Compared with that of the A356 aluminum alloy matrix, the hardness of the composite material greatly improved. The hardness of the composite prepared at 750℃ reached 245.6 HV, which was much higher than the 76 HV hardness of A356.

(3) The friction coefficient of the A356/3 wt.% Al$_3$Zr composite is lower than that of the A356 alloy. The bearing capacity of Al$_3$Zr particles stabilizes the performance of the composite under friction. For composite materials, the average friction coefficient is the lowest, 0.367, when the rotation speed is 250 rev/min and the load is 5 N.

(4) Compared with the A356 alloy, the A356/3 wt.% Al$_3$Zr composites experience less wear, have better wear resistance and have a relatively clean worn surface. The wear extent increases with increasing load and rotational speed, and the effect of the load on the wear rate is more obvious. For composites, the wear mechanism changes from adhesive wear and fatigue wear to delamination wear as the load increases. With increasing rotational speed, the wear mechanism changes from adhesive wear to abrasive wear.

Acknowledgment

References

1. M. Emamy, S.V. Yeganeh, A. Razaghian and K. Tavighi, Microstructures and Tensile Properties of Hot-extruded Al Matrix Composites Containing Different Amounts of Mg2Si, *Mat. Sci. Eng. A-Struct.*, 2013, **586**, p 190–196

2. S.L. Zhang, X.X. Shi, Y.T. Zhao, B.R. Zhang, Z.P. Liang, H.S. Yin, B.Y. Dou, Q. Zhang and C.X. Wang, Preparation of Microstructures and Mechanical Properties of in situ (TiB$_2$+ZrB$_2$)/AlSi$_9$Cu$_3$ Composites, *J. Alloy Compd.*, 2016, **673**, p 349–357

3. S. Khoramkhorshid, M. Alizadeh, A.H. Taghvaei and S. Scudino, Microstructure and Mechanical Properties of Al-based Metal Matrix Composites Reinforced with Al$_{84}$Gd$_6$Ni$_7$Co$_3$ Glassy Particles Produced by Accumulative Roll Bonding, *Mater. Des.*, 2016, **90**, p 137–144

4. X. Kai, K. Tian, C. Wang, L. Jiao, G. Chen and Y. Zhao, Effects of Ultrasonic Vibration on the Microstructure and Tensile Properties of the Nano ZrB$_2$/2024Al Composites Synthesized by Direct Melt Reaction, *J. Alloy. Compd.*, 2016, **668**, p 121–127

5. H.-J. Yang, Y.-T. Zhao, G. Chen, S.-L. Zhang and D.-B. Chen, Preparation and Microstructure of in-situ (ZrB$_2$ +Al$_2$O$_3$ +Al$_3$Zr)$_p$/A356 Composite Synthesized by Melt Direct Reaction, *Trans. Nonferrous Met. Soc. China.*, 2012, **22**(3), p 571–576

6. A. Omyma El-Kady, Fathy, Effect of SiC Particle Size on the Physical and Mechanical Properties of Extruded Al Matrix Nanocomposites, *Mater. Des.*, 2014, **54**, p 348–353

7. M. Sharitabar, A. Sarani, S. Khorshahian and M.S. Afarani, Fabrication of 5052Al/Al$_2$O$_3$ Nano Ceramic Particle Reinforced Composites via Friction Stir Processing Route, *Mater. Des.*, 2011, **32**(8), p 4164–4172

8. A. Canakci, Microstructure and Abrasive Wear Behaviour of B$_4$C Particle Reinforced 2014 Al Matrix Composites, *J. Mater. Sci.*, 2011, **46**(8), p 2805–2813

9. Z. Zhihao, Z. Yutao, K. Xizhou, T. Ran, D. Renfa and L. Liang, Hot Deformation Behavior and Processing Map of in-situ nano ZrB$_2$ Reinforced AA6111 Matrix Composites, *Mater. Res. Express*, 2019, **6**(2), p 1–11. https://doi.org/10.1088/2053-1591/aaed02

10. S.H. Seyed Ebrahimi, M. Emamy, N. Pourkia and H.R. Lashgari, The Microstructure, Hardness and Tensile Properties of a New Super High Strength Aluminum Alloy with Zr Addition, *Mater. Des.*, 2010, **31**(9), p 4450–4456

11. G. Manchang, J. Jun, L. Peijie, C. Yuyong 合金元素对铸造Al-Si-Cu-Mg合金机械性能的影响 (The Influences of Alloying Elements on the Mechanical Properties of Cast Al-Si-Cu-Mg Alloy), 材料科学与工艺 (Mater. Sci. Technol.), **1**(4), 73–79 (in Chinese) (1993)

12. B. Ravi, B. Balu Naik and J. Udaya Prakash, Characterization of Aluminium Matrix Composites (AA6061/B$_4$C) Fabricated by Stir Casting Technique, *Mater. Today-Proc.*, 2015, **2**(4–5), p 2984–2990

13. M. Esmaily, N. Mortazavi, J.E. Svensson, M. Halvarsson, M. Wessén, L.G. Johansson and A.E.W. Jarfors, A New Semi-solid Casting Technique for Fabricating SiC-Reinforced Mg Alloys Matrix Composites, *Compos. Pt. B-Eng.*, 2016, **94**, p 176–189

14. M. Zabihi, M.R. Toroghinejad and A. Shafyei, Shear Punch Test in Al/Alumina Composite Strips Produced by Powder Metallurgy and Accumulative Roll Bonding, *Mat. Sci. Eng. A-Struct.*, 2016, **667**, p 383–390

15. M. Meng, G. Chen, Z. Zhang and Y. Zhao, Analysis of Properties for in situ Al$_2$O$_3$p/A356 Composites Synthesised from the Al-SiO$_2$ System, *Mater. Sci. Technol.*, 2017, **18**(33), p 2290–2297

16. K.L. Tian, Y.T. Zhao, L. Jiao, S.L. Zhang, Z.Y. Zhang and X. Wu, Effects of in situ Generated ZrB$_2$ Nano-particles on Microstructure and Tensile Properties of 2024Al Matrix Composite, *J. Alloy. Compd.*, 2014, **594**, p 1–6

17. S.L. Zhang, J. Yang, B.R. Zhang, Y.T. Zhao, G. Chen, X.X. Shi and Z.P. Liang, A Novel Fabrication Technology of in situ TiB$_2$/6063Al Composites: High Energy Ball Milling and Melt in situ Reaction, *J. Alloy. Compd.*, 2015, **639**, p 215–223

18. Q. Gao, S. Wu, S. Lü, X. Xiong, R. Du and P. An, Improvement of Particles Distribution of in-situ 5 vol% TiB2 Particulates Reinforced Al-4.5 Cu Alloy Matrix Composites with Ultrasonic Vibration Treatment, *J. Alloy. Compd.*, 2015, **639**, p 215–223

19. S. Li, Y. Su, X. Zhu, H. Jin, Q. Ouyang and D. Zhang, Enhanced Mechanical Behavior and Fabrication of Silicon Carbide Particles Covered by in-situ Carbon Nanotubes Reinforced 6061 Aluminum Matrix Composites, *Mater. Des.*, 2016, **107**, p 130–138

20. Z.L. Liu, Chap 3, 摩擦学原理 (Principles of Tribology), First edition, Beijing, Higher Education Press, 2009, p 57–79

21. D.-B.Chen, X.-Y. Huo, S.-L. Zhang, Y.-T. Zhao (2008) (Al$_2$O$_3$+Al$_3$Zr) p/Al-22Si 铝基复合材料的制备及摩擦学性能(Fabrication and Tribological Properties of in situ (Al$_2$O$_3$+Al$_3$Zr)p/Al-22Si Composites), 机械工程材料 (Mater. Mech. Eng.), **32**(12), 47–50+58 (in Chinese)

22. A. Kumar, R.K. Gautam and R. Tyagi, Dry Sliding Wear Characteristics of in situ Synthesized Al-TiC Composites, *Compos. Interfaces*, 2016, **23**(6), p 469–480

23. F. Chang, Gu. Dongdong, D. Dai and P. Yuan, Selective Laser Melting of in-situ Al$_4$SiC$_4$+SiC Hybrid Reinforced Al Matrix Composites: Influence of Starting SiC Particle Size, *Surf. Coat. Technol.*, 2015, **272**, p 15–24

24. J. Teng, H.-P. Li and G. Chen, Wear Mechanism for Spray Deposited Al-Si/SiCp Composites Under Dry Sliding Condition, *J. Cent. South Univ.*, 2015, **22**(08), p 2875–2882

25. J. Lei, Z. Yutao, Y. Houshang, Z. Yang and Z. Jiayu, 锻压对原位 Al$_3$Ti/6063Al 复合材料微结构及摩擦磨损性能的影响(Effects of Forging on Microstructure and Friction and Wear Properties of Al$_3$Ti/6063Al in-situ Composites), *Rare Metal Mat. Eng.*, 2016, **45**(09), p 2391–2396. (**in Chinese**)

26. I. Barin and O. Knacke, *Thermochemical Properities of Inorganic Substance*, Springer, New York, 1973, p 792

27. H. Zhu, C. Jar, J. Song, J. Zhao, J. Li and Z. Xie, High Temperature Dry Sliding Friction and Wear Behavior of Aluminum Matrix Composites (Al3Zr+α-Al2O3)/Al, *Tribol. Int.*, 2012, **48**, p 78–86

28. K. Huang, R.-P. Jiang, X.-Q. Li, R.-Q. Li, L.-H. Zhang (2019) 超声外场对原位TiB$_2$/2A14 铝基复合材料的摩擦磨损性能的影响 (Effects of Ultrasonic Field on Friction and Wear Properties of in-situ TiB$_2$/2A14 Composite Materials), 材料工程 (J. Mater. Eng.), **47**(12), 78–84 (in Chinese)

29. Xu. Li Hui, J.L. Pinyi and Lu. Shengbo, Preparation and Mechanical and Tribological Properties of Al$_3$Zr+6082Al Composites Fabricated by Magnetic Stirring in situ, *Mater. Res. Express*, 2019, **6**, p 1–8

30. Y.Z. Zhang, *Chap 6,* 材料的干摩擦 (Dry Friction of Materials), 2nd ed. Science Press, Beijing, 2012, p 172

31. C. Zou, Z. Chen, H. Kang, W. Wang, R. Li, T. Li and T. Wang, Study of Enhanced Dry Sliding Wear Behavior and Mechanical Properties of Cu-TiB$_2$ Composites Fabricated by in situ Casting Process, *Wear*, 2017, **392**, p 118–125

32. Xu. Li Hui, J.L. Pinyi and Lu. Shengbo, Surface Wear Behavior and Strengthening Mechanism of Al$_3$Zr Particle Reinforced Aluminum Matrix Composites Prepared in situ, *Surf. Topogr.-Metrol. Prop.*, 2019, **7**, p 1–13